Data-Driven Analytics: A Novel Approach to Performance Diagnosis Using SpatioTemporal Analysis in a Giant Field Offshore Abu Dhabi

Mohamed Mehdi El Faidouzi and Djamel Eddine Ouzzane, ADNOC Offshore

Abstract

The field of data-driven analytics and machine learning is rapidly evolving today and slowly beginning to reshape the petroleum sector with transformative initiatives.

This work describes a heuristic approach combining mathematical modeling and associated data-driven workflows for estimating reservoir pressure surfaces through space and time using measured data. This procedure has been implemented successfully in a giant offshore field with a complex history of active pressure management by water and gas.

This practical workflow generates present-day pressure maps that can be used directly in reservoir management by locating poorly supported areas and planning for mitigation activities. It assists and guides the history matching process by offering a benchmark against which simulated pressures can be compared. Combined with data-based streamlines computation, this workflow improves the understanding of fluid flow movements, help to identify baffles and assists in field sectorization.

The distinctive feature of this data-driven approach is the unbiased reliance on field-observed data that complements complex modeling and compute-intensive schemes typically found in reservoir simulation. Conventional dynamic simulation and the tracing of streamlines require adequate static (e.g. permeability tensor) and dynamic models (e.g. pressures for each active cell in the system).

Alternatively data-driven streamlines are readily available and calibrated.

This paper presents innovative algorithms and workflows to the relatively limited existing body of literature on data-driven methods for pressure mapping.

In this case study, new insights are effectively revealed such as inter-reservoir communication, enabled a better understanding of the gas movement and supported the change in production strategy.

The paper is organized as follow. After a general overview of the field studied, this paper describes in detail the workflows used to interpolate pressures in space and time along with cross-validation results. Various applications of the pressure predictions are presented in the sections thereafter.

Field Overview

The giant oil field under consideration is located offshore Abu Dhabi and covers an area of approximately 40 by 25 km. The structure is a low-relief anticline with a dip varying from 1 to 4°. The fault pattern is

dominated by steep NW-SE strikes with less abundant NE-SW strikes. The fault throws are generally small and most faults are unlikely to be sealing laterally. The present-day SHmax in NNE- SSW direction will tend to potentially jack-open fractures and faults of similar orientation.

The oil accumulation is separated by dense argillaceous limestones into three distinct, stacked reservoirs (A, B and C) about 20 to 35 ft thick each (Fig. 1). Formation pressure tests showed overall a good vertical pressure communication intra-reservoir. Occasionally, especially towards the North and East, a generally tight clay-prone lithology forms a localised barrier between the upper and basal layers of reservoirs A and B as seen in Fig. 1. This paper will examine the case of the upper layers of reservoir A in particular, although the workflows developed are equally applicable to other reservoir zones.
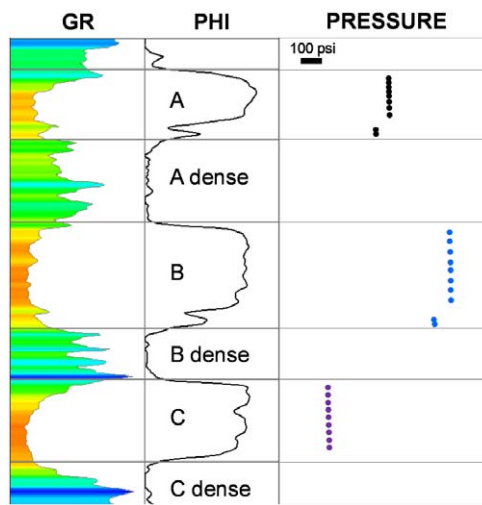

Figure 1—Typical log (gamma ray and porosity) and pressure profile across the reservoirs A through C.

Reservoir A is a laterally extensive porous carbonate deposited in a shallow water environment. Floatstones and rudstones form the main lithofacies with permeabilities ranging from 10 to 100 mD. Occasional occurance of grainstones locally boosts permeabilities above 100 mD. A pronounced porosity decrease is observed at down-flank wells and is interpreted to be due to a combination of poorer facies, degradation due to depth and increased diagenesis in the water leg.

Commercial production started in the late 1960s. After an initial period of natural depletion, various pressure maintenance strategies were deployed with dumpflood (1972 to 1984), peripheral water injection (from 1979) and crestal gas injection (from 2005).

Spatio-Temporal Analysis of Pressure Data

Prediction of spatial random fields based on observations at some set of locations is a common task in geostatistics and arises in geology, mining, hydrology and atmospheric sciences. Kriging procedures (Journel and Huijbregts 1978) are routinely being used to make optimal predictions at unsampled locations.

For quantities that vary in space and time, such as reservoir pressure, spatio-temporal interpolation can provide more accurate predictions than purely spatial interpolation because observations at other times are being considered. Several texts lay down the theoretical foundations of the emerging field of spatio-temporal statistics, specifically those of Cressie and Wikle (2011) and Sherman (2011). The spatio-temporal kriging techniques have been applied to a broad range of dynamic data including daily temperatures (Hengl et al. 2012), air pollution (Szpiro et al. 2002) and soil moisture (Heuvelink 1997).

In producing oil and gas assets, reservoir pressure measurements are made at a much higher frequency in the time domain compared to the spatial domain which requires additional wells to be drilled. The conventional approach of using a spatial interpolation (inverse distance weighted, kriging) based on a certain

time period misses on this valuable information and could potentially result in inconsistencies between maps from one time period to the next. In this case study, we present a heuristic approach to estimating reservoir pressure maps in reservoir A based on spatio-temporal interpolation. First reservoir pressure is modeled using smooth functions that capture the global trends while preserving the spatial and temporal continuity of pressure and pressure gradient. The residuals can be described by a stationary and spatially isotropic process. Residuals can then be predicted at unsampled space and time locations by kriging.

Pressure Global Trend using Generalized Additive Model
More than 3000 validated reservoir pressure data points have been measured at 260 wells in reservoir A throughout its 50 years of production. These pressures were determined by means of static gradient surveys, pressure transient analysis (PBU and PFO) and formation pressure tests. Fig. 2 shows the data coverage at different times with globally high pressures measured at peripheral water injectors and low pressures at producers located in the West.
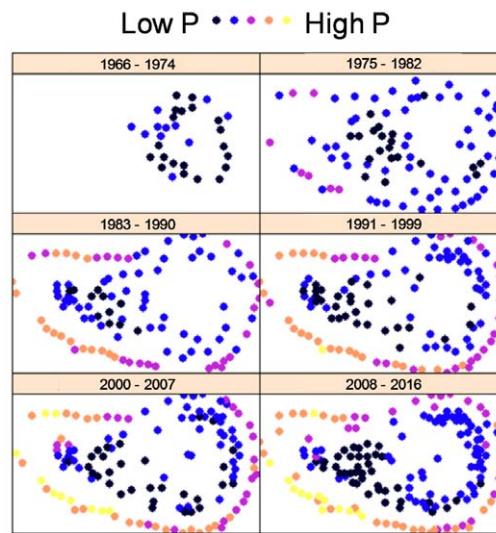

Figure 2—Treillis plot showing pressure data coverage and values at different time periods.

The field has a drop-shaped low-relief anticline, with a rounded dome-like eastern part and an elongated flatter western part (Fig. 3). In order to capture the field geometry and pressure characteristics (East and West), a quasi-cylindrical coordinate system combining true vertical depth and angle was adopted.
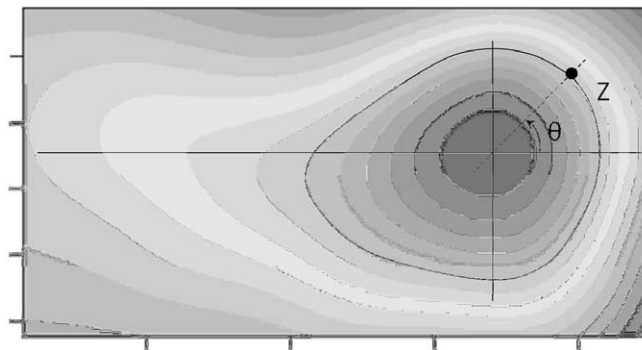

Figure 3—Quasi-cylindrical coordinate system combining true vertical depth (Z) and angle (0).

A correlation matrix was computed to explore the relationship between pressures and other variables (Fig. 4). The variables that were analyzed include time variables (date, development phase), geometry

(depth, angle) and well type. The Pearson correlation coefficient which measures the linear correlation indicated that pressure is highly correlated with the well type (0.79) and depth (0.63). A closer look at the bivariate scatterplot (Fig. 5) revealed non-linear U-shape behavior of pressure with depth. Other important relationships, not captured by the Pearson correlation, are the combined time/depth, and angle/depth correlation with pressure. Indeed throughout history, pressure around injectors tended to increase while pressures updip declined or remained stable. Also pressure differential between injectors and producers is lower in the East (low angle) compared to the West. This low differential in the East is indicative of a good pressure communication between injectors and producers.
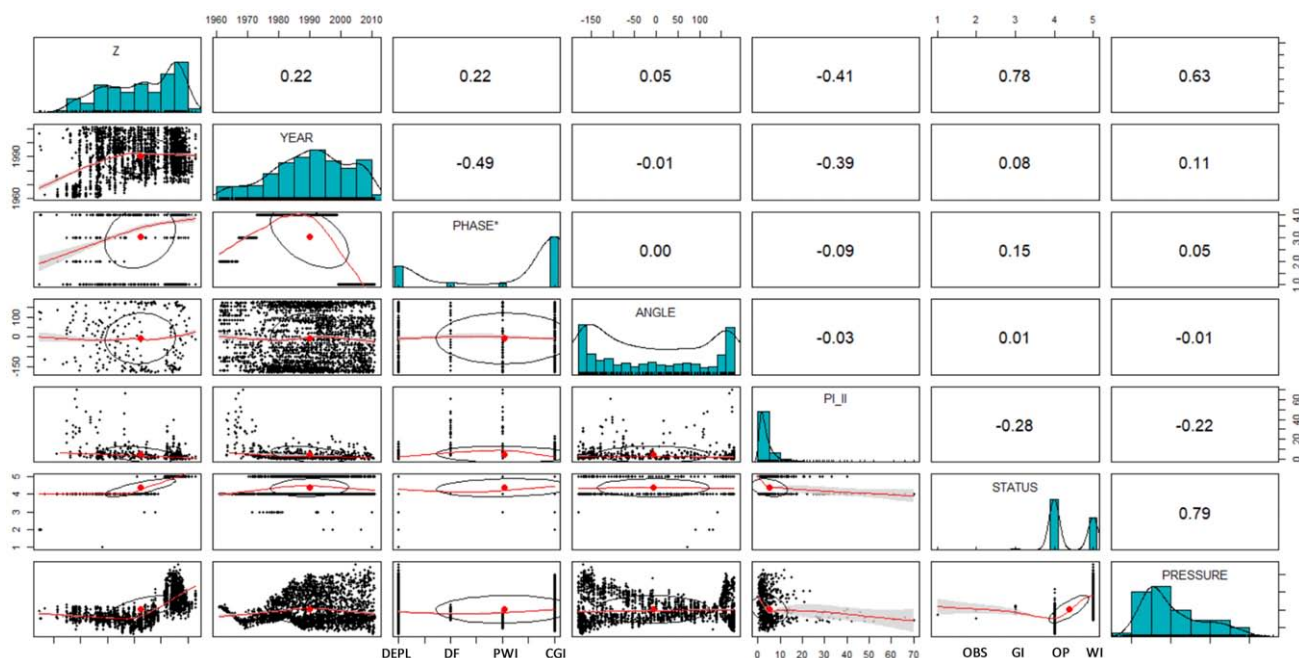
Figure 4—Correlation matrix showing in the last line, from left to right, the relationship between pressure and depth, time, development phase (DEPL=depletion, DF=dump flood, PWI=powered water injection, CGI=crestal gas injection), angle, productivity/injectivity index and well type (OBS=observer, GI=gas injector, OP=oil producer, WI=water injector).
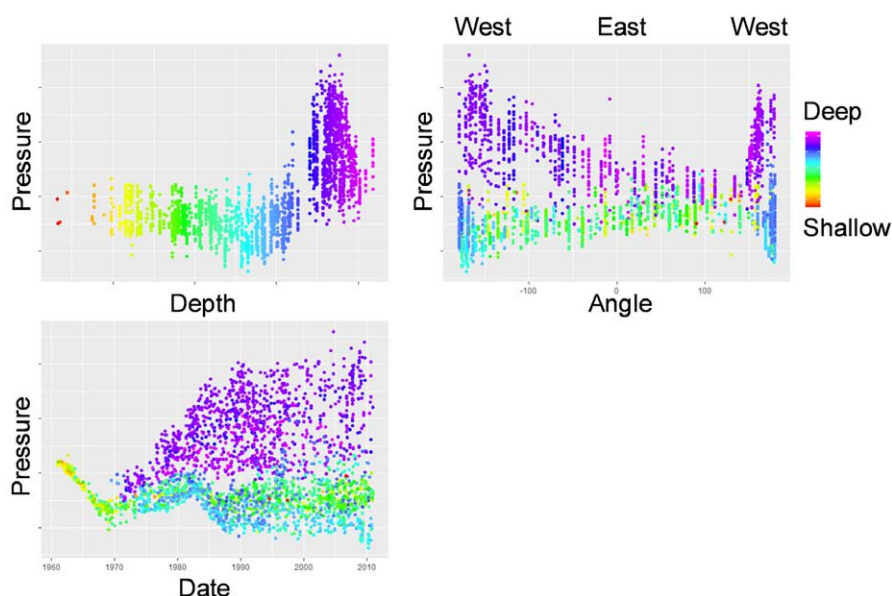
Figure 5—Detailed bivariate scatter plot of pressure vs depth (top left), angle (top right) and time (bottom left).

Based on this analysis, pressure can be modelled as a parametric function of time/depth and angle/depth. To capture the globally smooth spatial and temporal variation of pressure, Generalized Additive Models (GAMs) were employed. GAMs, originally developed by Hastie and Tibshirani (1990), are flexible and smooth estimators which capture non-linear relationships using basis functions which can be splines, polynomials or step functions. In GAM, the response *y* can be written as a function of the predictor variable *x* plus some error ε as follow:

$$y = f(x) + \varepsilon = \sum_{j=1}^{d} B_j(x)\, \gamma_j + \varepsilon$$

where each B_j is a pre-defined basis function and γ_j the corresponding regression coefficients determined by penalized regression.

In the case of reservoir pressure, the choice of predictors and basis functions was through trial and error. The model that best fit the data with the lowest degree of freedom is a sum of tensor products; using Duchon splines for depth and time, and cyclic splines for angle to guarantee continuity:

$$p(\mathbf{x},t) = f(z \otimes t) + g(z \otimes \theta) + \varepsilon$$

Fig. 6 shows the goodness of fit of the GAM pressure predictor. The model degrees of freedom (mdf) are equal to 39 for 2843 observations. It is worth noting that an mdf of 2 is a straight line while an mdf approaching the number of observations would over-fit the data and produce 'wiggly' surfaces. The model explains 87% of the variability and the standard deviation of the residuals is 280 psi.
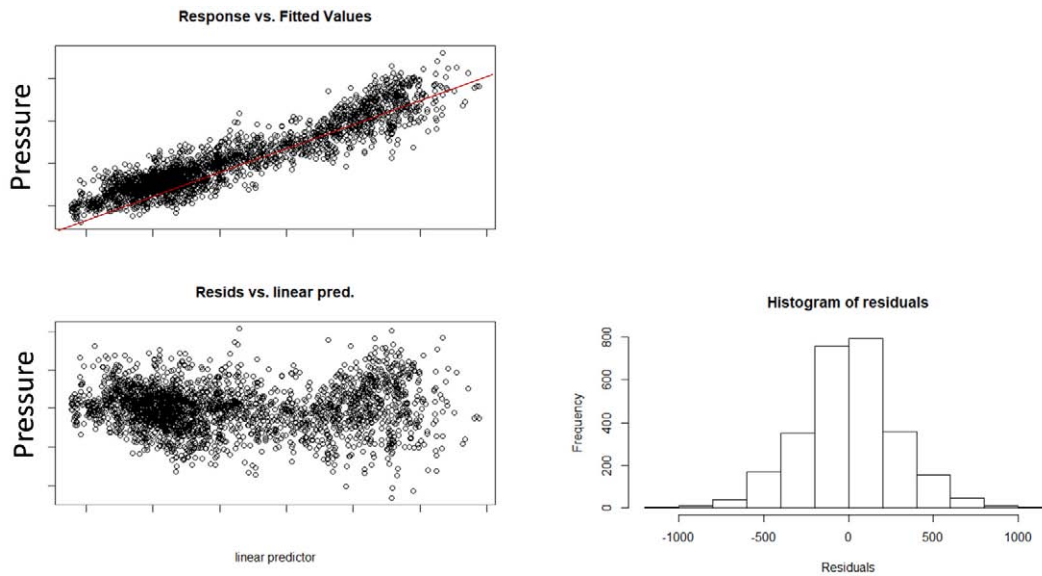

Figure 6—Goodness of fit of the GAM pressure predictor.

Smooth surfaces of pressure as a function of time and depth can now be generated for different areas of the field. Fig. 7 shows the computed pressure surface and reveals a complex structure. The pressure response in the West differs from the pressure response in the East with an apparent pressure baffle at mid-depth that started in the 1980s. This corresponds as we will see later to the dumpflood effect. Pressure maps were generated yearly; some of which are shown in Fig. 8.
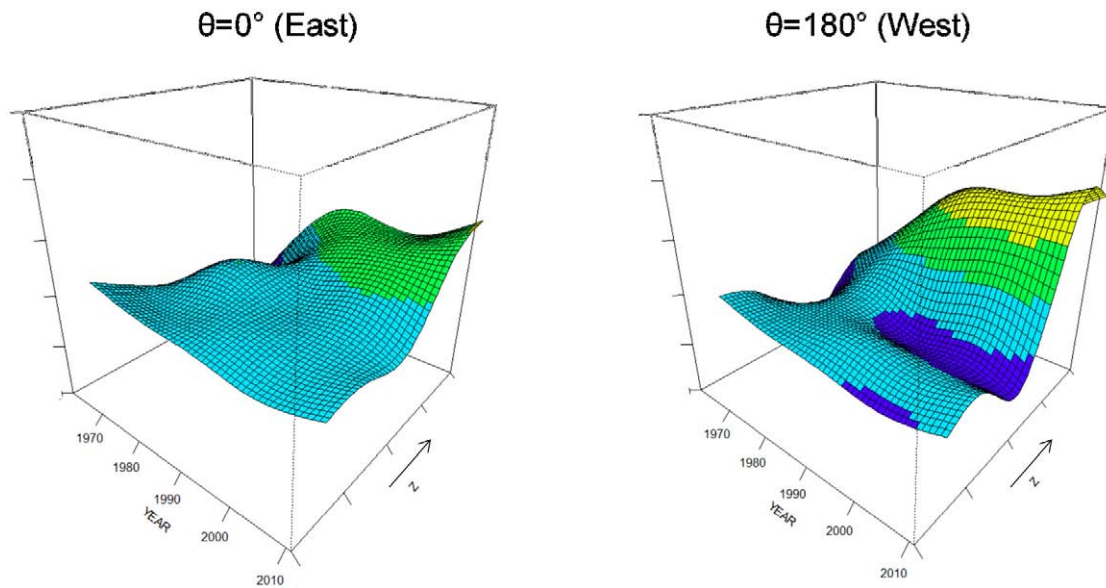
θ=0° (East)   θ=180° (West)

Figure 7—Surface of pressure as a function of time and depth in the East (left) and West (right)

Low P ▆▆▆▆▆▆▆▆▆▆ High P

1970   2000

1980   2010
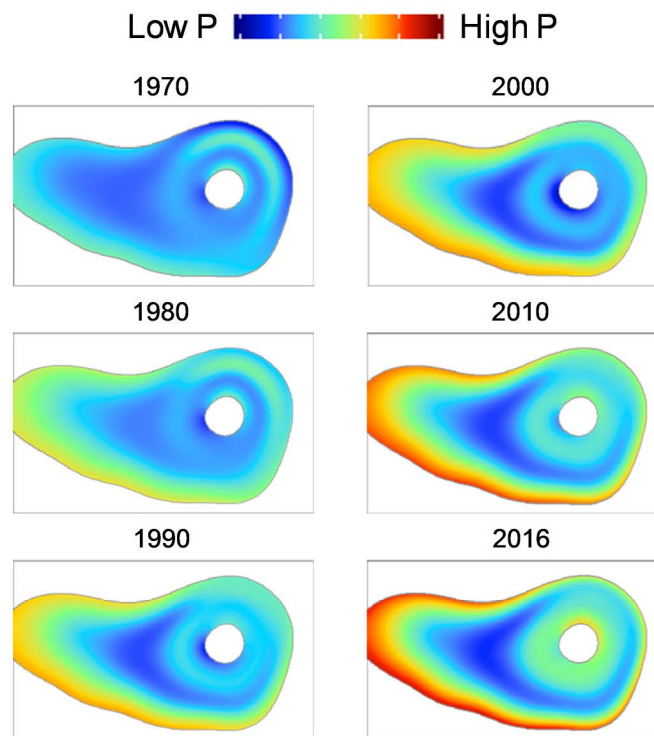
1990   2016

Figure 8—Pressure maps from the GAM predictor.

Pressure Local Trend using Spatio-temporal Kriging

So far a global trend of pressure was obtained, however detailed reservoir performance and baffle identification requires capturing local trends. As seen in Fig. 9, residuals are uncorrelated with time and position. The Q-Q plot in Fig. 10 indicates that the residuals are normally distributed. Fig. 11 also reveals that residuals are not geographically clustered.
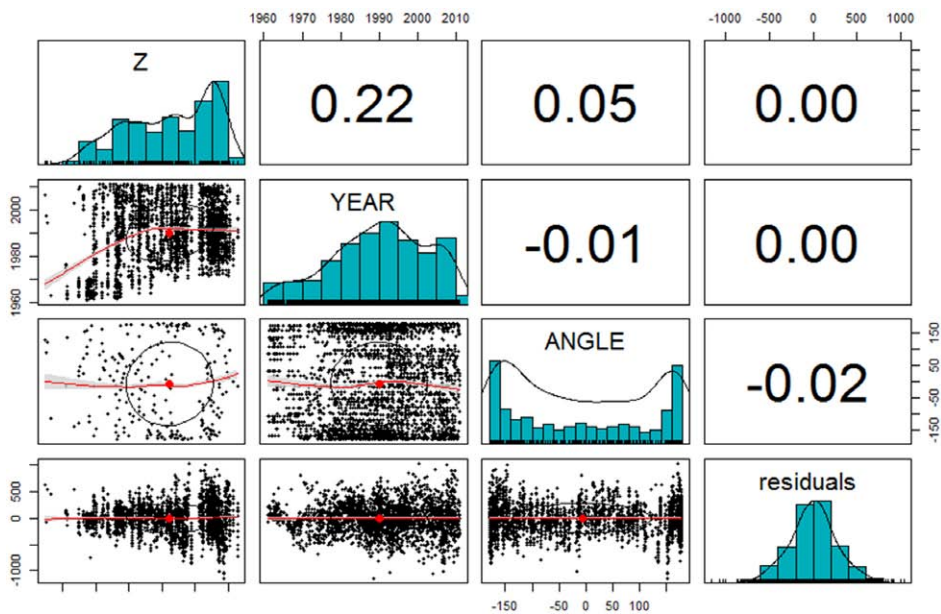
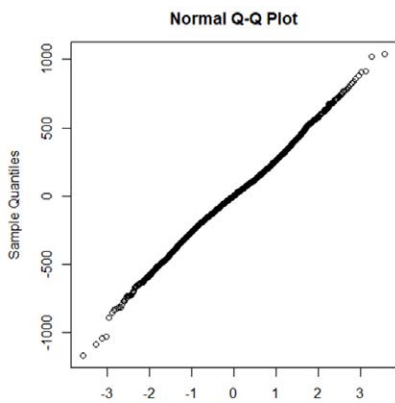**Figure 9—Correlation matrix of the residuals.**

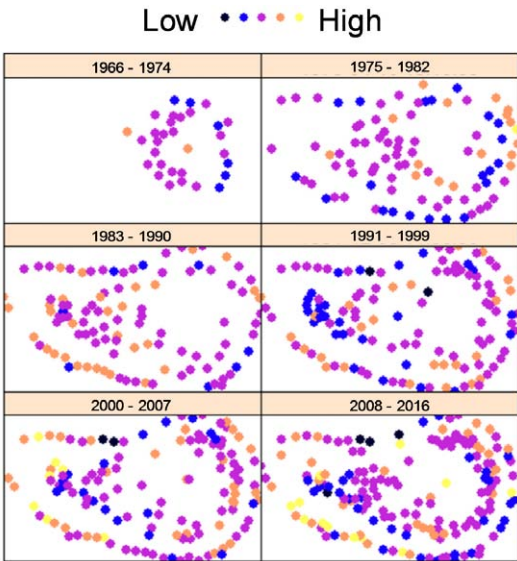**Figure 10—Q-Q plot for the residuals.**

Figure 11—Treillis plot showing residuals at different times.

The spatial as well as temporal continuity of pressure (and residuals) steers us towards spatiotemporal kriging whereby near and recent observations are more correlated than distant ones. More rigorously it can be said that for a Gaussian stationary and isotropic random field r, in this case pressure residuals, the covariance between two points only depends on their spatial separation h and their temporal separation u. The empirical variogram can then be defined analogously to that in the purely spatial case:

$$\gamma(h,u) = \frac{1}{2|N(h,u)|} \sum_{N(h,u)} \left(r(x_i, t_i) - r(x_j, t_j) \right)^2$$

where $N(h, u)$ are all the pairs of points distant by h in space and u in time.

The empirical variogram surface for pressure residuals was computed over a distance of 10 km and a time lapse of 5 years using regular binning intervals of 1 km and 1 year. Fig. 12 shows the empirical variogram along with the proposed best fitting separable model variogram for reservoirs A and B. The separable model is the simplest covariance model and assumes separability between the spatial and the temporal component, meaning that the covariance function is given by:
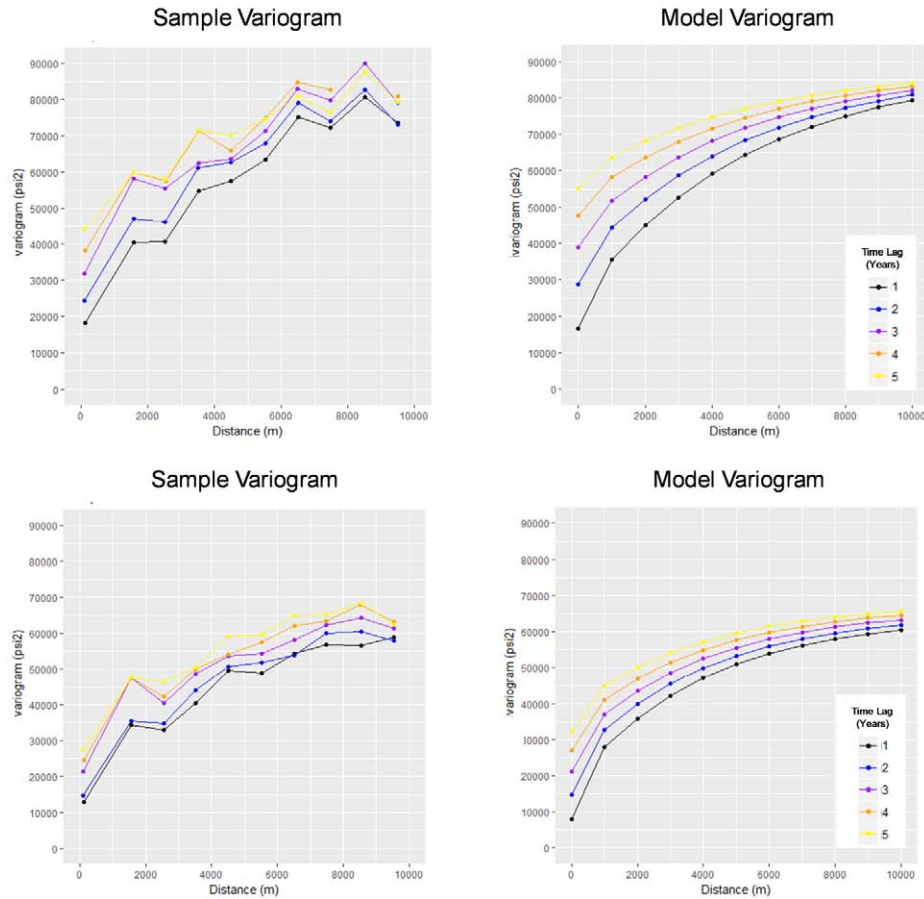
$$C(h,u) = C_s(h) \cdot C_t(u)$$

Figure 12—Sample (left) and the best fitting separable spatio-temporal variogram (right) for reservoir A (top) and reservoir B (bottom).

The best fitting parameters used are summarized in Table 1. The temporal range of 9.5 years for reservoir A implies that the temporal correlation is very strong. Reservoir B, which is of better reservoir quality, has wider drainage areas at producers and experiences a better pressure support as it takes up most of the injected water. These characteristics can explain the lower degree of pressure variability (i.e. lower residual

sill) and more prominent temporal correlation (i.e. larger residual time range). The model spatial range of 4 km is much higher than the estimated average well drainage area of less than 1 km and must be interpreted as the size of the regions where pressures tend to cluster rather than a single well influence radius.

Table 1—Separable model best fitting parameters for reservoirs A and B.
Both the spatial and temporal variograms use the exponential model (Exp).

reservoir	domain	partial sill	model	range	nugget	sp-temp sill
A	space	0.9	Exp	5 km	0.10	$295\ psi^2$
	time	1.1	Exp	9.5 yr	0.03	
B	space	0.7	Exp	4 km	0.14	$270\ psi^2$
	time	1.3	Exp	19 yr	0.01	

Residuals maps can be generated by spatio-temporal kriging using the separable model. The interpolation is based on a reduced kriging neighbourhood to reduce the computation associated with the full kriging predictor and relax the assumption of stationarity. We are now in the position to interpolate reservoir pressure at unobserved locations in space and time using the GAM predictor p_{GAM} and the residual r:

$$p(\mathbf{x},t)=p_{GAM}(\mathbf{x},t)+r(\mathbf{x},t)$$

Fig. 13 shows how the global smooth pressure prediction is transformed to reveal local intricate pressure distortions.
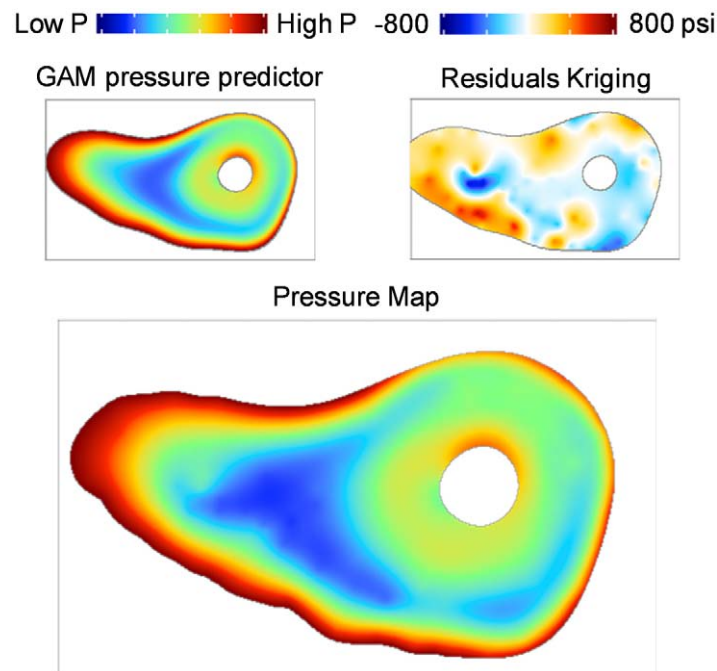

Figure 13—Pressure map in 2016 (right) obtained from GAM pressure predictor (left) and residuals kriging (center).

Blind Test

In order to test the pressure interpolation workflow, five producers (OP1 to OP5) and one injector (WI1) spread across the field were selected for a leave-one-out cross-validation. Each time the kriging prediction of residuals is based on all observation wells except for one and a pressure history prediction is generated for that well. For OP5 only a subset of pressure observations was removed to test the ability of the workflow to fill gaps in time series.

Fig. 15 shows the observed and predicted pressure history for these wells. As expected the GAM predictor captures the broad pressure trends with decreasing pressures at OP1, stable pressures at OP5 and increasing trends for OP2, OP3, OP4 and WI1. The kriging greatly improves the quality of the match by grasping the local higher frequency non-monotonic trends.
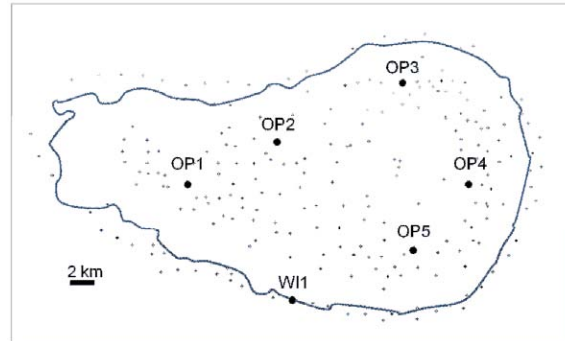

Figure 14—Location of the five producers (OP1 to OP5) and water injector (WI1) used in the blind test.
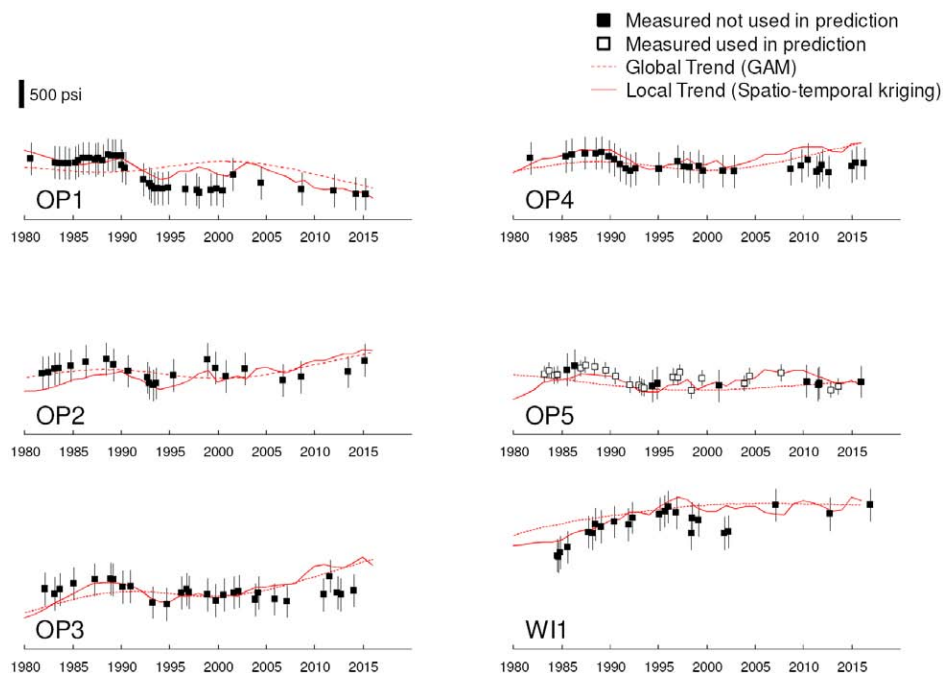

Figure 15—Measured (black squares) and predicted evolution of reservoir pressure at five blind test wells using GAM (dotted red) and spatio-temporal kriging (continuous red). The error bars are 300 psi for unused pressure data and 150 psi for used pressure data (approximate variability predicted by the spatio-temporal nugget).

The average RMSE for all wells except OP5 is 60 psi. For OP5 the RMSE is lower at 54 psi. This blind test showed that this workflow combining smooth functions and spatio-temporal kriging can accurately predict pressures at untested locations and fill gaps in time series.

Applications to Reservoir Diagnostic

Accurate data-driven prediction of pressures has a broad range of applications, from history matching benchmarking to data acquisition planning to pressure communication and fluid flow characterization.

This section will succinctly describe each of these examples.

History Matching Benchmark

The history matching workflow typically starts with dynamic pressure match under liquid voidage control followed by fractional flow match under oil rate control and requires most of the time iterations between these two steps. The pressure match QC is commonly presented in the form of pressure time series at well level and sometimes region level. The drawback of this approach is the lack of spatial understanding of the mismatch area and clustering.

Conversely data-driven pressure maps can conveniently be compared with simulation based pressure maps to identify areas of poor match. The added value vis-a-vis well by well QC plots is the spatial dimension which allows trends to be identified. For example Fig. 16 unveils a pressure depletion area in the West larger and more pronounced than predicted by the simulation model.
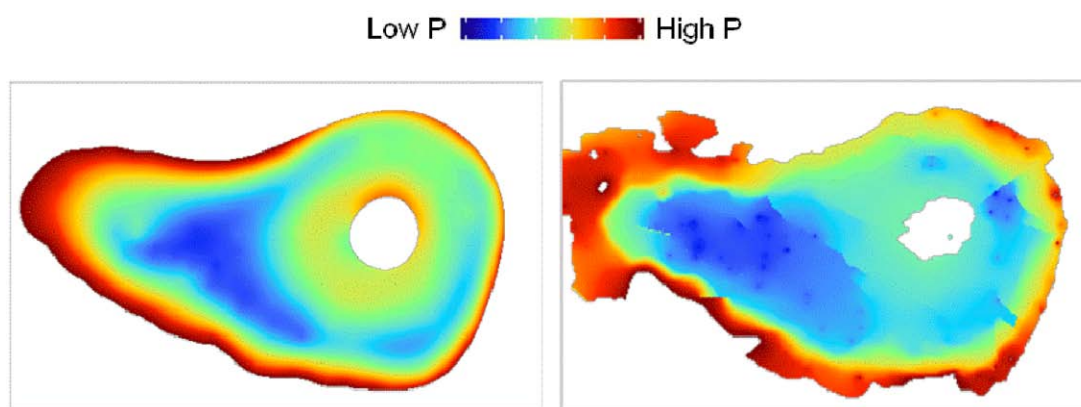

Figure 16—Data-driven pressure map generated using the spatio-termporal analysis (left) and simulated pressure map (right) at the same time step.

Optimization of pressure data acquisition

It is necessary to understand the uncertainty associated with the data-driven pressure predictions in order to plan the drilling of new in-fills and optimize the data acquisition plan. The square root of the kriging variance at the last time step (Fig. 17) gives an idea about the areas where standard deviation exceeds 300 psi, mostly located away from pressure control points. Combined with a pressure time derivative map (Fig. 17) that shows areas where pressures vary the most, it can be a powerful tool for optimizing the pressure data acquisition plan. More observations would be required in areas where uncertainties are high or where pressure is changing fast.
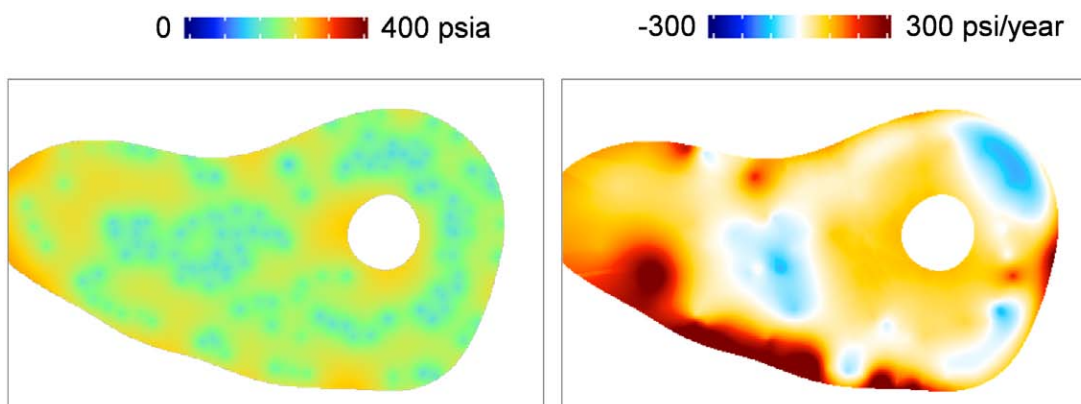

Figure 17—Standard deviation map of the residuals (left) and pressure time derivative (right) in 2016.

Inter-reservoir differential pressure analysis

The pressure mapping process was repeated for reservoir B. Pressure differential between reservoir A and B is shown at at different time steps in Fig. 18. Due to its more favorable reservoir property and smaller aerial extent, reservoir B is generally overpressured compared to reservoir A.
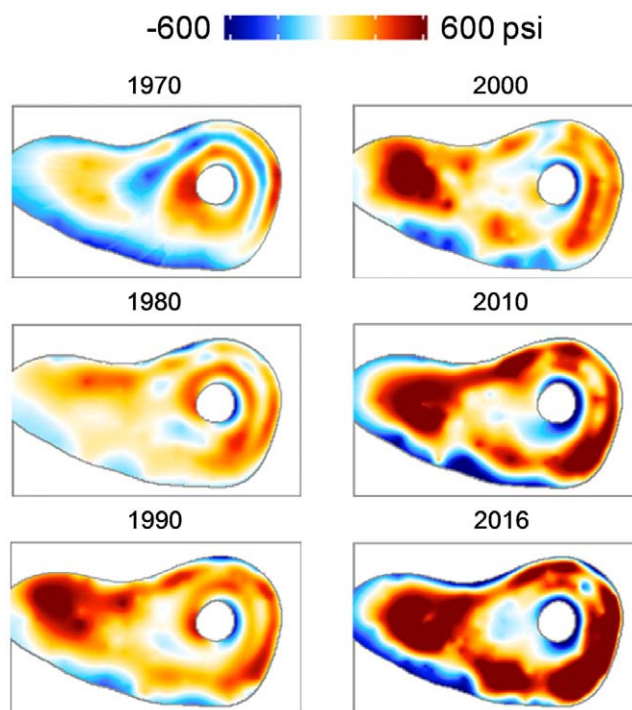

Figure 18—Pressure differential between reservoir A and B. Areas in red are regions where pressure in B is higher.

In order to reduce noise the absolute differential pressure was averaged across the last 5 years in Fig. 19. Areas of consistently low differential pressure can potentially be a sign of genuine reservoir communication through faults, or simply a localized artifact caused by an integrity issue at the tested well, bearing no relation to the reservoir. In the present case the pressure anomalies do not align along faults. In fact the differential pressure is higher than 100 psi throughout the field with the exception of the area marked [a] where it ranges from 20 to 50 psi. In this particular region the lack of coverage is such that the uncertainty is too high (Fig. 17) to make any sort of conclusion.
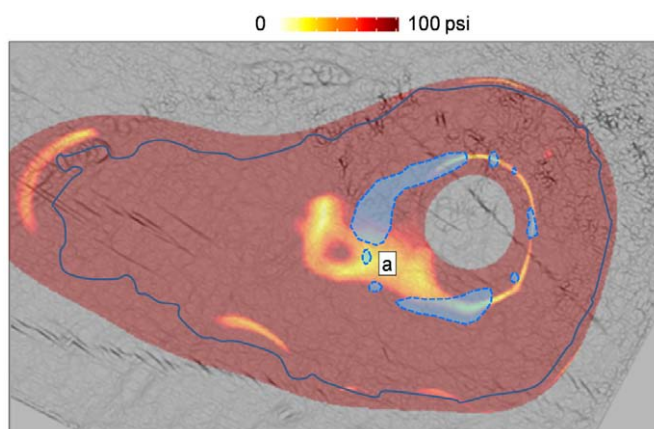

Figure 19—Average absolute differential pressure between reservoir A and B in the last 5 years. Background map is the seismic curvature attribute map highlighting the major faults. The blue shaded areas correspond to areas where dumpflood water was injected.

As a result differential pressure did not show any prospect of inter-reservoir communication.

Data-Driven Streamlines

Another area of application is the understanding of fluid movement through the computation of streamlines. Data-driven streamlines were computed from the pressure maps and the productivity /injectivity index interpolation map using the approximation:

$$\mathbf{q} = -c\, \frac{K\, k_r}{\mu} \vec{\nabla}(p_r + p_c - \rho g h) \propto -\mu_{\text{ratio}}\, PI\, \vec{\nabla}p$$

The gas being five times less viscous than the oil at reservoir condition, a viscosity ratio term p_{ratio} was introduced to account for it.

The pressure streamlines are shown in Fig. 20. At the crest [a], the viscous pressure gradients are below 0.1 psi/ft much lower than the gas/oil gravity gradient of 0.16 psi/ft. The dominant gravity force explains the gas gravity override observed from saturation time-lapse at crestal wells. On the flanks, the pressure gradient is quite variable. The NE region [b], rich in grainer facies, has a weak pressure gradient around 0.1 psi/ft relative to the oil/water gravity gradient of 0.21 psi/ft which supports the gravity dominated saturation profile observed at some wells. The southern region [c], of poorer reservoir quality, has a strong viscous gradient of 0.2 to 0.35 psi/ft and many wells display a piston-like displacement. In some instances the vertical heterogeneity distorts the shape of the waterfront movement, despite the favourable mobility ratio, and fingering takes place.
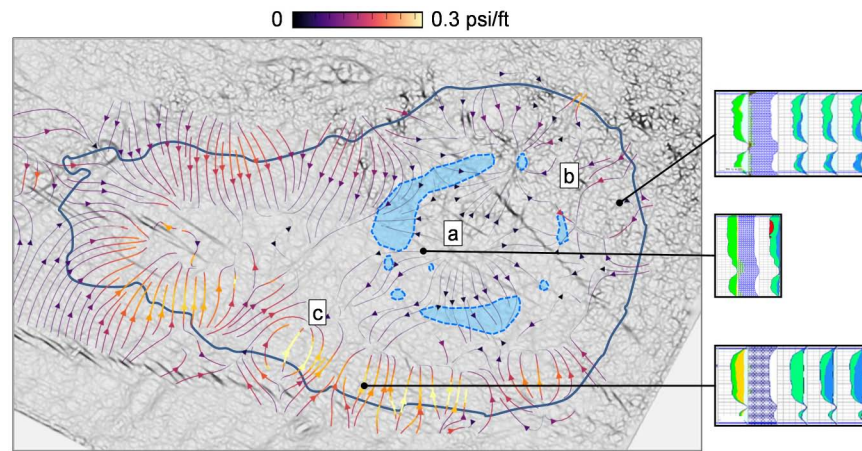

Figure 20—Data-driven pressure gradients in 2016. The thickness of the streamlines is proportional to the pressure gradient. Time lapse saturation logs for selected wells are presented on the left.

The flux streamlines are shown in Fig. 21. The flux at the crest [a], representing the gas movement, is consistent with the GOR trend and highlights a dominant SW direction of the gas expansion. Also abrupt termination or change of direction of streamlines, as in [b], coincides with the dumflood area which acts as a barrier. Similarly a sharp reduction in intensity is seen in area [c]. The reasons for this high gradient could include a locally poor reservoir quality between injectors and producers, the close presence of en echelon faults preventing the dissipation of pressure south towards the aquifer.
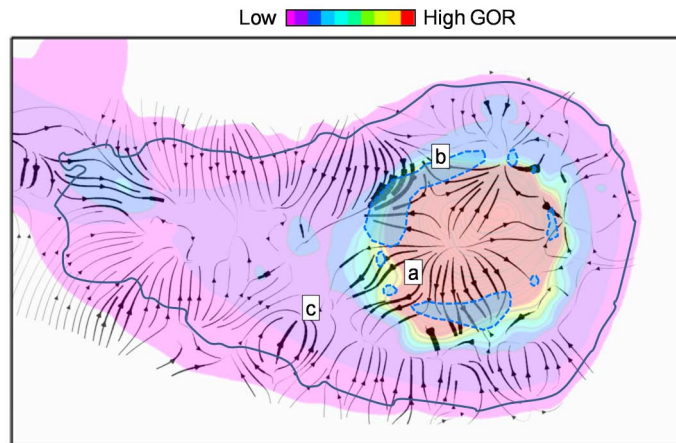
Figure 21—Data-driven streamlines in 2016. The background map is an interpolation of GOR based on flow tests.

Lagrangian Coherent Structures

The streamlines display in Fig. 20 provides a notion of the overall transport due to viscous forces. A drawback of this visualization is that it takes an instantaneous view of the velocity vector field. Additionally, streamlines are sensitive to short-term perturbations and small-scale noise. In the case of a dynamic reservoir system with changes in fluxes, shifts in development strategy and continuous drilling, the velocity vector field is time-dependant. Thus streamlines, which would need to be applied to isolated time steps, are not suited to analyse time-dependent dynamics.

In recent years, many of the recently developed methods for the analysis and visualization of fluid flow time-dependent vector field topology are related to Lagrangian coherent structures (LCS). LCS introduced by Haller (Haller 2001) separate regions of qualitatively different flow behavior. Examples of LCS in nature include eddies in oceanography and hurricanes in meteorology. This section discusses the applicability of the LCS concept to the reservoir flow, in particular for the detection of barriers.

A popular method to identify LCS is the finite-time Lyapunov exponent (FTLE) method (Peacock and Dabiri 2010). The FTLE measures the Lagrangian separation by determining the growth of the distance between particles during their travel over a finite time. The particles can be moved forward (foreward FTLE) or backward (backward FTLE) in time. The forward FTLE identifies ridges of repelling LCS; in the case of reservoir flow these would signal barriers where incoming streamlines separate away (Fig. 22). The backward time identifies attracting LCS which indicate areas of high influx where streamlines tend to converge.
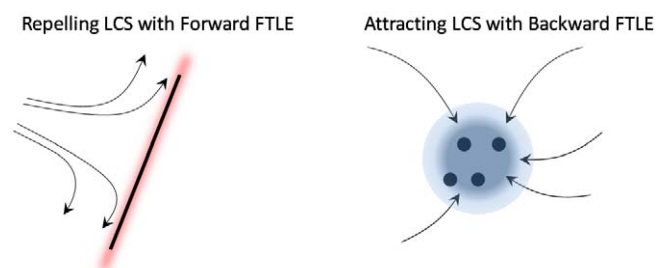

Figure 22—Illustration of LCS in the case of Forward FTLE (left) and Backward FTLE (right).

The computation of FTLE was done with different integration time corresponding to the main development phases (Fig. 23). During the early depletion and dumpflood phase, the NE region [a] had a large backward FTLE indicating a larger depletion. During peripheral and crestal gas injection, areas [a],

[b] and [c] display a large forward FTLE. As mentioned before [a] is a dumpflood area. The LCS confirms what has already been observed from streamlines with the added benefit of delivering sharper images.
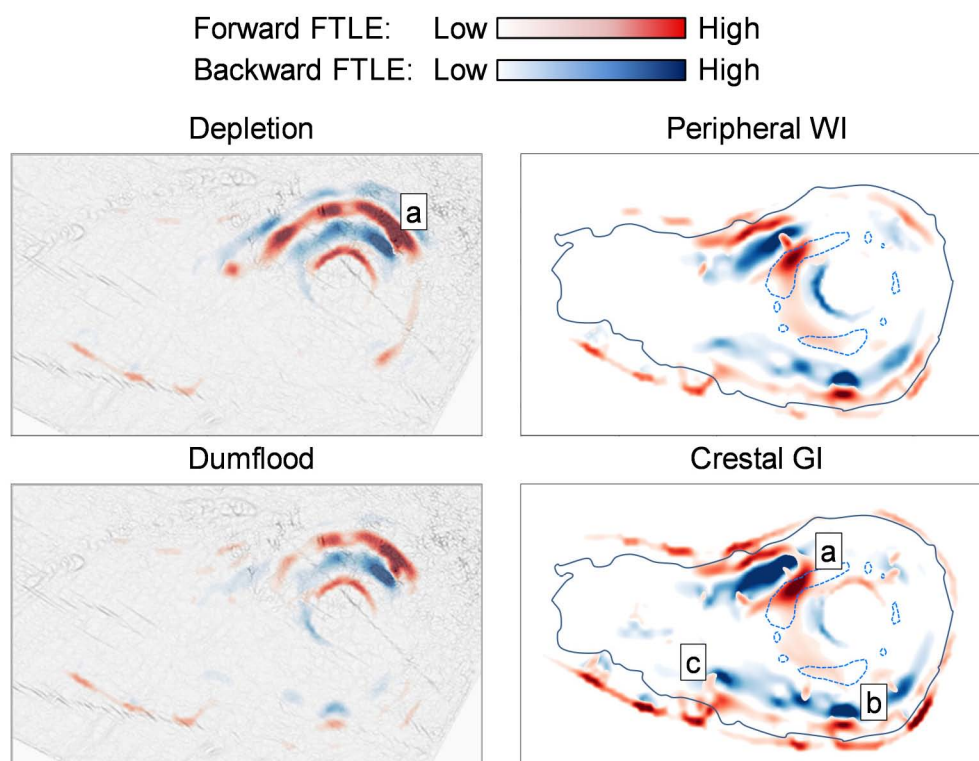

Figure 23—Pathline-based FTLE forward (red) and reverse (blue) integrated across different development phases.

Conclusion

This paper introduced a novel workflow for generating pressure maps from measured data using generalized additive model for large scale trends and spatio-temporal kriging of residuals for small scale features. This practical workflow can be used directly in reservoir management by locating poorly supported areas and planning for mitigation activities

The developed method was successfully implemented in an offshore field with complex geological features as well as a long history of pressure maintenance schemes. The method was found very valuable in guiding the process of history matching in such giant field by offering a benchmark against which simulated pressures can be compared.

The new workflow improves the understanding of fluid flow movements, helps to identify baffles and assists in field sectorization especially when combined with data-based streamlines computation. Such understanding is paramount in deriving the best reservoir management guidelines for reservoir energy conservation and increased production.

Acknowledgments

Nomenclature

   c = conversion factor, 0.001127 bbl/D.cp.ft.mD^{-1}.ft^{-2}.psia^{-1}
   C = spatio-temporal covariance

C_s = spatial covariance term
C_t = temporal covariance term
g = acceleration constant, 32.174 ft/s^2
h = thickness of the reservoir, ft
K = absolute permeability, mD
k_r = relative permeability of the phase under consideration
p = reservoir pressure at datum depth, psia
p_c = capillary pressure, psia
p_r = reservoir pressure at depth, psia
$\mathbf{q}$ = flux (flow rate per unit cross sectional area vector), bbl/D/ft^3
r = residual pressure, psia
t = time, year
$\mathbf{x}$ = UTM coordinates, m
z = reservoir depth, ft

greek letters

γ = variogram
ε = error, psia
θ = angle in pseudo-radial coordinates, degrees
μ = viscosity of the phase under consideration, cp
μ_{ratio} = ratio of the viscosity of the phase under consideration to the oil viscosity, cp
ρ = density of the phase under consideration, lbm/ft^3

mathematical operators

A = gradient operator
$\otimes$ = tensor product

Subscripts

GAM = Generalized Additive Model

Reference

Cressie, N. and Wikle, C. 2011. *Statistics for Spatio-Temporal Data*. Chicester, UK: John Wiley and Sons Ltd.

Graler, B., Pebesma, E. and Heuvelink, G. 2016. Spatio-Temporal Interpolation using gstat. *RFID Journal* **8** (1): 204–218.

Hastie, T. J. and Tibshirani, R. J. 1990. *Generalized Additive Models*. New York: Chapman & Hall/CRC.

Hengl, T., Heuvelink, G. B. M., Percec Tadic, M. and Pebesma, E. J. 2012. *Theoretical and Applied Climatology* **107** (1-2): 265–277. http://doi.org/10.1007/s00704-011-0464-2

Heuvelink, G. B. M., Musters, P. and Pebesma, E. J. 1997. Geostatistics Wollongong **2**: 1020–1030.

Journel, A. G. and Huijbregts, C. J. 1978. *Mining Geostatistics*. London: Academic Press.

Peacock, T. and Dabiri, J. 2010. Introduction to Focus Issue: Lagrangian Coherent Structures. *Chaos* **20** (1).

Pebesma, E. J. 2004. Multivariable geostatistics in S: the gstat package. *Computers & Geosciences* **30** (7): 683–691. http://doi.org/10.1016/j.cageo.2004.03.012

Sherman, M. 2011. *Spatial Statistics and Spatio-Temporal Data: Covariance Functions and Directional Properties*. Hoboken, USA: John Wiley & Sons, Ltd.

Szpiro, A. A., Sampson, P. D., Sheppard, L., Lumley, T., Adar, S. D. and Kaufman, J. D. 2010. Predicting intra Durban variation in air pollution concentrations with complex spatioD temporal dependencies. *Environmetrics* (21): 606–631. http://dx.doi.org/10.1002/env.1014

Wood, N. S. 2017. *Generalized Additive Models: An Introduction with R, Second Edition*. New York: Chapman and Hall/CRC.